



# Population scaling biases in map samples of power-law fault systems

T. Manzcchi<sup>a,\*</sup>, J.J. Walsh<sup>a</sup>, W.R. Bailey<sup>b</sup>

<sup>a</sup> Fault Analysis Group, UCD School of Geological Sciences, University College Dublin, Dublin 4, Ireland

<sup>b</sup> Woodside Energy Ltd, 240 St George's Terrace, Perth, WA 6000, Australia

## ARTICLE INFO

### Article history:

Received 21 December 2007

Received in revised form

2 June 2009

Accepted 4 June 2009

Available online 13 June 2009

### Keywords:

Fault populations

Power-law

Size bias

Censoring bias

## ABSTRACT

Fault population power-law exponents derived from maps are subject to sampling biases, yet simple methods do not exist for estimating quantitatively the unbiased population characteristics from the measured (biased) ones. Fault length, maximum throw and geometric moment populations measured in different sized maps of the same natural fault system are used to test new analytical results. In the analytical treatment, scale-specific probability density functions of the different measures of fault size are derived by calculating the probability of sampling faults censored to particular sizes within a small-scale sample area of a power-law population. The best-fit power-law exponents of these analytically biased populations match closely the average exponents observed at the same scales in both natural and synthetic fault maps. The exponents are less at smaller scales, with the maximum throw population showing the greatest bias and the length population the least. Exponents deduced from fault maps representative of many published ones are unlikely to be biased by more than 0.1 for the length population, but scaling biases of 0.3 or more are likely for maximum throw populations. Population exponents measured at particular scales can be used to estimate those at different scales using a maximum likelihood estimation procedure.

© 2009 Elsevier Ltd. All rights reserved.

## 1. Introduction

Fractures often occur in populations with power-law size distributions, and departures from this ideal are generally attributed to influences of mechanical layering or the free surface (e.g. Marrett et al., 1999; Ackermann et al., 2001; Gillespie et al., 2001; Soliva and Benedicto, 2005). Graphical methods for plotting and interpreting power-law size data, and relationships linking population characteristics measured in different sample dimensions have been available for some time (e.g. Heffer and Beven, 1990; Marrett and Allmendinger, 1991; Walsh et al., 1991, 1994; Westaway, 1994; Pickering et al., 1995, 1996; Bonnet et al., 2001). This status is reflected by the declining academic interest for characterising fault and fracture size populations *per se* since the thematic double-issue of the Journal of Structural Geology devoted to the topic (Cowie et al., 1996). Fault populations are still of strong practical significance since they underpin fault and fracture network modelling methods for the petroleum, groundwater and mining industries (e.g. Maerten et al., 2006; Ortega et al., 2006; Barr, 2007; Dee et al., 2007; Mäkel, 2007; Manzcchi et al., 2008), as well as providing insight into fault system evolution and

localisation (e.g. Meyer et al., 2002; Hardacre and Cowie, 2003; Walsh et al., 2003b; Moriya et al., 2005). Therefore advances in understanding and characterising scaling systematics of power-law fault systems remain important.

The purpose of the current work is to understand why the scale-specific average values of power-law exponents of fault populations measured in different sized maps of the same fault system appeared to decrease with scale. Specifically, is this effect evidence of natural non-power-law fault scaling in a dataset championed for its power-law faults (Watterson et al., 1996; Bailey et al., 2005), or is it some form of sampling bias? The question is tackled algebraically, and the core of this paper is a derivation of probability density functions (pdfs) of fault size (length, maximum throw and geometric moment) in areal sub-samples of idealised power-law systems. This derivation is of interest since the approach can be modified for other problems, however the results of the derivation (i.e. the pdfs) confirm that observed scaling biases should, indeed, be expected. The results are generalised as look-up charts of bias in power-law exponent as a function of map size, the resolution of the smallest mapped faults, and the characteristics of the unbiased, power-law fault system.

Lastly, these analytical results deriving from consideration of idealised fault systems are tested for a natural system. A maximum likelihood estimation of the unbiased fault system characteristics for the natural system based on the populations measured at one

\* Corresponding author. Tel: +353 1 716 2606; fax: +353 1 716 2607.  
E-mail address: [tom@fag.ucd.ie](mailto:tom@fag.ucd.ie) (T. Manzcchi).

scale is obtained. The populations measured at other scales are then compared to those predicted from this estimate using the new analytical results.

## 2. Fault populations in the East Pennines Coalfield

### 2.1. The dataset

The East Pennines Coalfield (EPC) pseudo-seam map (e.g. Watterson et al., 1996; Bailey et al., 2005) derives from a compilation of 1:2500 scale seam abandonment plans in an approximately 1300 km<sup>2</sup> area of the Westphalian Pennine Basin of North England (Fig. 1a). The abandonment plans record the boundaries of workings, seam elevations, fault traces and throws for all worked areas, which often include vertically stacked seams. Slip vectors for individual faults are not recorded on the plans, but field evidence suggests that most of the faults, which dip around 70°, are pure dip-slip (Walsh and Watterson, 1988a). A few WNW-striking, dextral strike-slip fault zones post-date the normal faults (Watterson et al., 1996; Bailey et al., 2005), and only the vertical component of displacement (i.e. the fault throw) is recorded for these, as well for the dip-slip faults.

The map is based as far as possible on plans for an extensively worked seam (the Barnsley/Top Hard), but data from higher or lower seams were projected to this level to fill gaps between workings, providing an areally extensive map of fault traces and throws. Details of the construction of the pseudo-seam map, which is estimated to have a lateral resolution of the fault traces of ca. 10 m, are given by Watterson et al. (1996) and Bailey et al. (2005). Various aspects of the fault system have also been described by Walsh and Watterson (1988b, 1990), Gillespie et al. (1992), Clark et al. (1999), Bailey et al. (2002) and Walsh et al. (2003a).

The fault resolution of the abandonment plans, and hence of the pseudo-seam map, is variable and depends primarily on the vintage of the plans. Resolution in the 87 km<sup>2</sup> area studied by Watterson et al. (1996) is greater than average and faults as short as 200 m, and with maximum throws as small as 60 cm, are included. The resolution for maximum throw in the map as a whole is approximately 1 m, and this map version (Fig. 1a) contains only faults with maximum throws greater than this value. Individual faults have throw values recorded at between 2 and 77 positions along their trace, and the 5297 faults are characterised by 40577 throw values.

The smallest recorded throws on individual traces are between 10 cm and 50 cm, and faults are therefore not mapped to their tips (i.e. positions of zero throw). Tip resolution effects can significantly influence fault-trace length populations, and dataset-specific corrections are required (e.g. Walsh and Watterson, 1988b; Heffer and Beven, 1990; Yielding et al., 1996). For the present analysis, each fault was extended by 125 m per tip (250 m per fault), consistent with the value determined for the EPC faults by Watterson et al. (1996) and Bailey et al. (2005).

### 2.2. Definitions, assumptions and terminology

Three measures of fault size are used in this paper, fault-trace length, maximum fault throw and geometric moment. Fault-trace length ( $L$ ) includes the tip-correction of 125 m per tip. The maximum fault throw ( $T_{\max}$ ) is not necessarily located at the centre of the fault trace and represents about 94% of the maximum fault displacement because most faults are normal dip-slip with a  $\approx 70^\circ$  dip. The geometric moment of a fault is the product of average displacement and fault surface area (King, 1978), and populations of geometric moment relate directly to the fault-induced strain (e.g. Scholz and Cowie, 1990; Marrett and Almendinger, 1991; Westaway,

1994). The two-dimensional, throw-based geometric moment measure used in this study is defined as:

$$M = \int_0^L T dL, \quad (1)$$

where  $T$  is the local throw.

This paper considers 2D map-samples of fault systems. A fault is considered in a sample if at least some of it is present. If a fault is not completely sampled, only the portion of its trace length and geometric moment contained in the sample area are considered. The point of maximum throw for an incomplete fault may or may not be in the sample area and if not, the maximum throw value considered is the maximum value present on the portion of fault trace contained in the area. Throughout this paper, we use the terms  $l$ ,  $u$  and  $m$  to signify the length, maximum throw and geometric moment of the portion of a fault contained in the area of interest, and reserve the terms  $L$ ,  $T_{\max}$  and  $M$  to refer to the length, maximum throw and geometric moment of entire faults (Table 1). The terms  $s$  and  $S$  are used as general expressions for, respectively, the sampled and total sizes of faults. Hence, if a fault is sampled completely,  $s = S$ , but otherwise  $s < S$ . No further assumptions are made in the analysis of the natural dataset, and the three size types ( $l$ ,  $u$  or  $m$ ) are considered independently. The algebraic treatments to follow, however, assume idealised systems in which  $L$ ,  $T_{\max}$  and  $M$  are linked explicitly.

For a system of randomly positioned faults with power-law sizes, a general expression of the number of faults with sizes between  $s$  and  $s + ds$  contained in an area  $A_1^2$  is given by:

$$n(s, A_1) = a_s A_1^2 s^{-c_s} ds \quad (2)$$

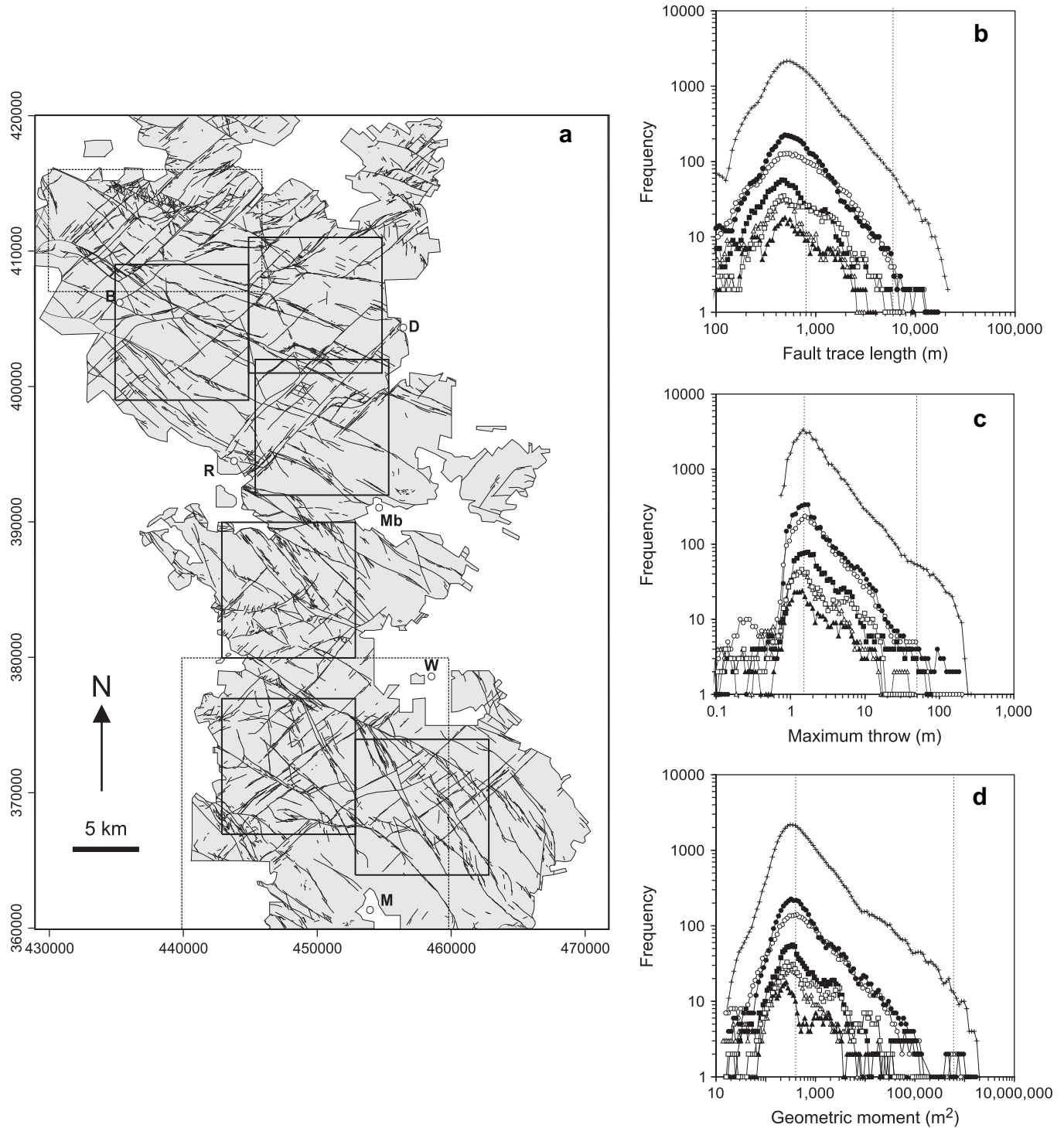
where constant  $a_s$  reflects the overall abundance of faults, and exponent  $c_s$  the relative frequencies of faults of different sizes (e.g. Davy, 1993; Berkowitz et al., 2000).

### 2.3. Scale-specific population exponents

The log-interval method (e.g. Pickering et al., 1995) is used to estimate power-law exponents,  $c_s$ , from the map samples (Fig. 1). The log-interval plot is essentially a histogram of the logarithm of fault size which is characterised by a linear trend between  $\log(\text{frequency})$  and  $\log(\text{size})$  with a slope of  $-(c_s - 1)$  for a power-law distribution. Overlapping bins are used in the histogram constructions, with the size of each bin set at 5% of the total scale-range of interest, and the spacing between the bin centres set at either 12.5% or 25% of the bin size.

The entire dataset shows reasonably tight power-law frequency distributions for length (Fig. 1b) with  $c_l = 2.76$  for  $800 \text{ m} < l < 6000 \text{ m}$ , for maximum throw (Fig. 1c) with  $c_u = 2.22$  for  $1.3 \text{ m} < u < 50 \text{ m}$  and for geometric moment (Fig. 1d) with  $c_m = 1.70$  for  $200 \text{ m}^2 < m < 600,000 \text{ m}^2$ . We defined six  $10 \times 10 \text{ km}$  areas with complete map coverage (Fig. 1a) and subdivided each into four  $5 \times 5 \text{ km}$  areas and sixteen  $2.5 \times 2.5 \text{ km}$  areas. We censored all faults at the edges of each area, and calculated  $c_l$ ,  $c_u$  and  $c_m$  by examining each log-interval frequency plot (two examples at each scale are shown in Fig. 1b–d), setting area-specific upper and lower size limits to the power-law portion of the sample population, and performing linear regression for that portion.

The variability in  $c_s$  as a function of map size is shown in Fig. 2. All populations included in this plot contain at least 25 faults and had correlation coefficients ( $R^2$ ) greater than 0.75. Of the 96  $2.5 \text{ km}$  areas, 66 length populations, 54 maximum throw populations and 61 geometric moment populations meet these conditions, as do all populations measured for larger areas. The exponents measured



**Fig. 1.** (a) Map of the East Pennines Coalfield showing all recorded faults with maximum throws > 1 m. Faults are mapped up to the edges of the mine workings, shown as the shaded area. Sample areas for the present analysis are shown as solid boxes. Dashed boxes show areas described by [Watterson et al. \(1996\)](#) in the north of the map and by [Bailey et al. \(2002\)](#) in the south. The circles show Barnsley (B), Doncaster (D), Rotherham (R), Maltby (Mb), Wakefield (W) and Mansfield (M). The map is referenced to the UK National Grid. Length (b), maximum throw (c) and geometric moment (d) populations for sample areas of the fault map. Each plot shows populations in the entire area (+), and for two 10 km × 10 km (○, ●), 5 km × 5 km (□, ■) and 2.5 km × 2.5 km (△, ▲) sub-areas. The dashed vertical lines indicate the size limits used to determine the population exponents for the entire area.

from the entire dataset are assigned a nominal sample size of  $A_1 = 45$  km in [Fig. 2](#). These exponents are consistently greater than the averages measured in the smaller sample areas, but this observation should be treated with caution since the exponents for the entire dataset derive from a highly irregular map ([Fig. 1a](#)) with extremely subjective boundaries (many of the mine

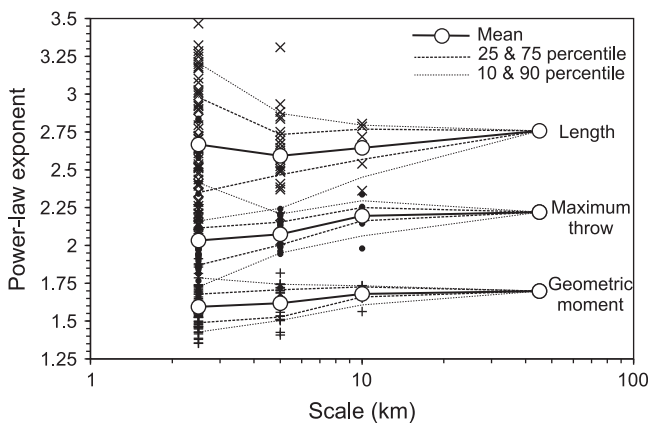
workings are bounded by large faults). In the smaller areas with complete map coverage, the length population exponent ( $c_l$ ) does not show a systematic trend with sample scale, and the scale specific mean value has a narrow range between  $2.59 \pm 0.28$  to  $2.67 \pm 0.4$ . In contrast, both mean  $c_u$  and mean  $c_m$  decrease with decreasing scale, with  $c_u$  ranging from  $2.19 \pm 0.12$  at 10 km, to

**Table 1**  
Nomenclature.

Symbol	Meaning
$A_0$	The edge of a large square map
$A_1$	The edge of a square area contained inside $A_0^2$
$L$	Fault-trace length
$T$	The throw at a position on a fault trace
$T_{max}$	The maximum throw on a fault trace
$M$	Fault geometric moment
$S$	General term for the total size of a fault ( $S$ is $L$ , $T_{max}$ or $M$ )
$l$	The length of the portion of a fault contained in $A_1^2$
$u$	The maximum throw on the portion of a fault contained in $A_1^2$
$m$	The geometric moment of the portion of a fault contained in $A_1^2$
$s$	General term for the size of the portion of a fault in $A_1^2$ ( $s$ is $l$ , $u$ or $m$ )
$B, n$	Constant and power-law exponent relating $T_{max}$ to $L$
$p(L, A_1 X)$	The conditional probability that a fault in $A_0^2$ is sampled in $A_1^2$ subject to censoring type $X$
$p(L \rightarrow s)$	The probability that a fault of total length $L$ is censored to a size $s$ in $A_1^2$
$n(S, A_0)$	The number of fault centres in $A_0^2$ with uncensored sizes in the range $S$ to $S+ds$
$n(s, A_1)$	The number of faults in $A_1^2$ with censored or uncensored sizes in the range $s$ to $s+ds$
$N(s, A_1)$	The cumulative number of faults in $A_1^2$ with sizes $\geq s$
$\bar{N}(s, A_1)$	The expected cumulative number of faults in $A_1^2$ with sizes $\geq s$
$f(s, A_1)$	The probability density function (pdf) of fault size in $A_1^2$
$a_L, c_L$	Frequency constant and power-law exponent of the distribution $n(L, A_0)$
$c_s$	The power-law exponent of the biased distribution $n(s, A_1)$
$\bar{c}_s$	The expected best-fit power-law exponent of $n(s, A_1)$ .
$\sigma_{c_s}$	The standard deviation of the distribution of $c_s$
$N$	The total number of faults in $A_1^2$
$\bar{N}$	The expected total number of faults in $A_1^2$
$s_{N(s, A_1)=1}$	The largest expected fault in $A_1^2$
$L_x$	A length term used in the analyses (see Table 2)
$L_{max}, L_{min}$	Maximum and minimum fault lengths present in $A_0^2$
$max_L, min_L$	Maximum and minimum fault lengths associated with specific types of censoring.

$2.03 \pm 0.26$  at 2.5 km, and  $c_m$  ranging from  $1.67 \pm 0.06$  at 10 km, to  $1.60 \pm 0.14$  at 2.5 km.

Two possible explanations exist for the decrease in mean exponent of the maximum throw and geometric moment populations with decreasing scale: bias on the estimation of the power-law exponent, and biases introduced by sampling. Pickering et al. (1995) investigated bias in estimating power-law exponents from natural and synthetic data. Although the log-interval method is in most cases the best approach, all methods are to some extent biased, producing an exponent which is progressively smaller for samples containing progressively fewer data. The bias is a consistent percentage of  $(c_s - 1)$  for a particular sample size, and, for our



**Fig. 2.** Population exponents for fault length (x), maximum throw (●) and geometric moment (+), for sample sub-areas. Also shown are the exponents measured in populations of the entire area (assigned a nominal scale of 45 km).

analysis, should therefore be a function of scale rather than population type. Since our subarea exponents do not show this relationship (Fig. 2), we infer that the scale-dependencies are instead caused by sampling bias.

**2.4. Sampling biases**

Four types of sampling bias are recognised: orientation, truncation, censoring and size (e.g. Zhang and Einstein, 2000). Orientation bias is the over or under sampling of fractures because of their orientation with respect to the orientation of the sample area. This bias is not responsible for the decreases in exponent value with decreasing sample-area size because the same orientation of samples is used at all scales.

Truncation bias refers to effects caused by a systematic under-representation of smaller faults in the sample. If the sample has a well-defined lower size limit, the limit of the power-law distribution is sharp on a log-frequency plot, and truncation does not cause a problem. For example, the throw cut-off applied during map construction yields a sharp lower limit to the maximum throw power-law distribution at 1.3 m (Fig. 1c). By contrast if smaller fractures are instead gradually under-represented rather than abruptly omitted, the effect of this under-representation is a gradual decrease in power-law slope. For example, the fault length population for the entire EPC (Fig. 1b), shows a gradual decrease in slope between about 800 m and 500 m before dropping off sharply below 500 m. For this population, therefore, the effective limit of the distribution occurs at 800 m, and inclusion of smaller faults in the analysis would result in the determination of a biased power-law exponent. For this case, truncation bias is avoided by selecting a lower size limit for the population which excludes the effects of the bias (e.g., Fig. 1b). The vertical lines in Fig. 1b–d indicate the size limits used to determine the power-law exponents for the entire EPC samples. For smaller sample areas, each sample was inspected visually to define sample-specific upper and lower size cut-offs between which the exponents were measured, eliminating truncation bias as a concern.

Censoring bias refers to incomplete sampling of individual faults because only a portion of the fault occurs in the sample area. Faults which are much smaller than the width of the sample are less likely to be affected by censoring, but the probability of sampling both fault tips decreases to zero as the fault length approaches the width of the sample area. Censoring bias therefore results in samples containing relatively fewer longer faults, and so results in artificially increased power-law exponents. Methods exist to estimate the distribution of total trace lengths from the censored distribution, for example the Kaplan-Maier method, which does not assume an underlying distribution (e.g. Laslett, 1982; Odling, 1997). It is sometimes assumed that the distributions deriving from such corrections (which have lower  $c_s$  than the censored distributions) should be representative of the size distribution for a larger area. However, since there is also greater probability of sampling longer faults in finite sample areas (size bias), this type of correction strategy for censoring bias would over represent the larger faults because it does not consider size bias (e.g. Yielding et al., 1996; Bonnet et al., 2001). Thus, we did not apply this correction strategy, but instead considered the implications of censoring and size biases simultaneously.

Censoring and size bias have opposing effects and therefore, must to some extent cancel each other. In the case of fault-trace length populations, available evidence suggests that they do so fairly effectively in many cases, implying that uncorrected populations measured in finite sample areas may have power-law exponents representative of the underlying population. For example, Yielding et al. (1996) measured length populations in



samples of an idealised power-law system, and found that the censored and size biased population exponent is close to the true value. For a fault trace map derived from seismic interpretation, Belfield (1992) found that the mean  $c_l$  of four sub-areas was the same as  $c_l$  in the whole area. Similarly, an approximately scale independent average  $c_l$  value is observed for the areas of the EPC with complete map coverage (Fig. 2). The greater value for  $c_l$  obtained from the whole map area compared to the scale-independent mean values for the complete smaller samples (Fig. 2) is consistent with a dominance of censoring bias over size bias in the incompletely sampled whole map arising from the large, but uneven, area of mine workings (Fig. 1). Given that for the maximum throw and geometric moment populations, the mean exponent decreases for smaller sample areas (Fig. 2), we infer that size bias is more important than censoring bias for populations of these measures of fault size.

Whilst it is desirable in practice to know whether a measured population exponent is biased and by how much, it is only of secondary interest to know the individual contributors to the total bias. For this reason, we focus in this paper on the total bias (i.e. including effects of both censoring and size bias) of population exponents, and use the term scaling bias to describe how the total bias changes in maps at different scales.

### 3. Analytical determination of biased fault populations

Our approach for assessing generally scaling biases on power-law fault population exponents is to derive probability density functions (pdfs) of fault size, which include the bias. An analytical derivation has advantages over numerical approaches because: (a) estimation bias is not present in characterising the distribution because it is calculated not estimated, (b) multiple realisations are not required since the pdf represents the ideal mean fault size distribution and (c) the pdf can be evaluated at different scales and for different large-scale systems to establish general trends in bias.

The idealised fault system geometry used in the analytical treatment is described in Section 3.1. In Section 3.2, a synthetic map constructed using the same assumptions is examined. Analysis of this map using the same methods as for the EPC map provides a benchmark against which the analytical results, derived in Section 3.3–3.7, can be checked (Section 3.8). Finally, in Section 3.9 the results of the analysis are discussed from the perspective of establishing what scaling biases in population exponent are likely to be present in map samples of a representative range of fault systems.

#### 3.1. Idealised fault system geometry

A power-law population of fault-trace lengths is assumed to be contained in a large square area of edge length  $A_0$ , and faults are assumed to be oriented with equal probability in one of the two orientations parallel to the edges of this area (Fig. 3a). The objective of the analysis is to derive the expected distributions of censored fault length, maximum throw and geometric moment ( $l$ ,  $u$  and  $m$ ) measured in a smaller area  $A_1^2$  contained within  $A_0^2$ .

Following Eq. (2), the number of fault centres contained in  $A_0^2$  which have uncensored lengths in the range  $L$  to  $L + dL$  is given by:

$$n(L, A_0) = a_L A_0^2 L^{-c_L} dL. \quad (3)$$

The length and maximum throw of the faults ( $L$  and  $T_{max}$ ) are linked through the usual expression (e.g. Gillespie et al.; 1992; Schultz et al., 2008):

$$T_{max} = BL^n, \quad (4)$$

where  $B$  and  $n$  are constants. We assume triangular throw profiles (e.g. Manighetti et al., 2001; Manzocchi et al., 2006) along the length of the fault traces, ranging from  $T=T_{max}$  at the centre of the trace to  $T=0$  at the two tip points. Therefore:

$$M = \frac{1}{2}LT_{max} = \frac{1}{2}BL^{n+1}. \quad (5)$$

These relationships between the various fault size measures (Eqs. (4) and (5)) were not assumed explicitly for the EPC populations in the previous section, but the EPC faults follow this scaling with scatter (Bailey et al., 2005). Manipulation of Eqs. (2)–(5) give the exponents of the maximum throw and geometric moment populations in  $A_0^2$ . These are:

$$c_{T_{max}} = (c_L + n - 1)/n \quad (6)$$

$$c_M = (c_L + n)/(n + 1) \quad (7)$$

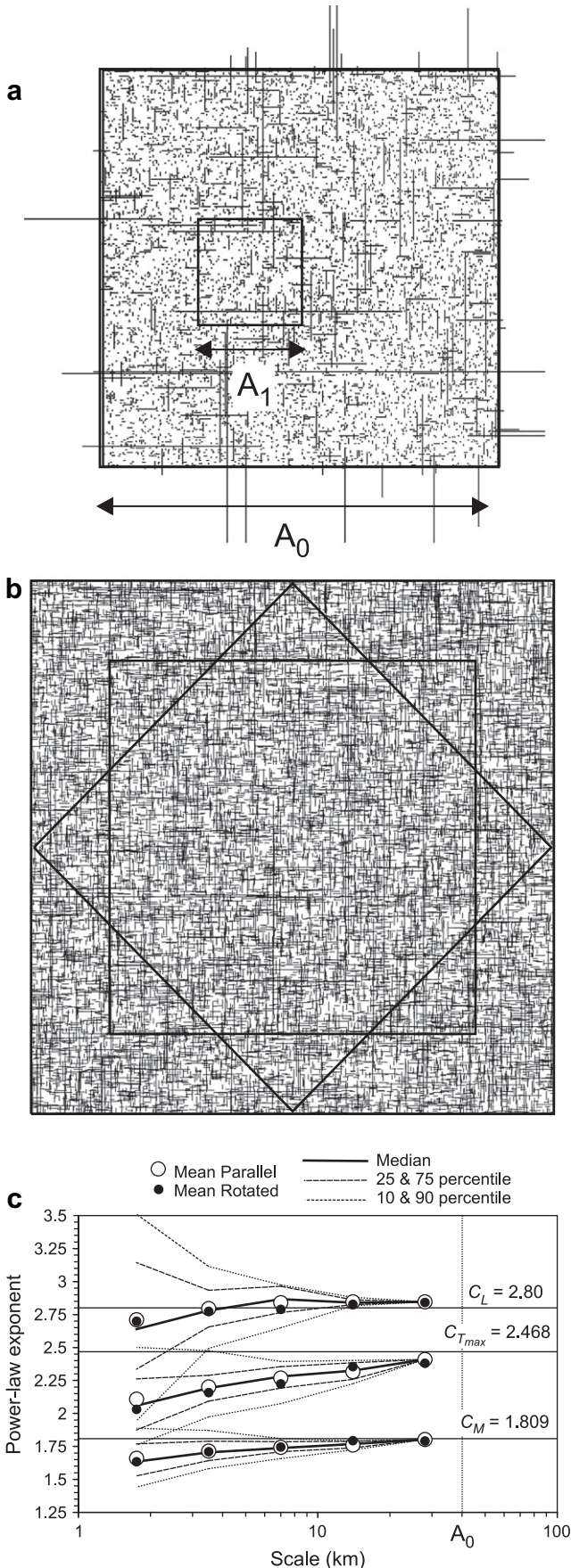
#### 3.2. Case example

A synthetic map (Fig. 3b) based on this idealisation was constructed accounting for edge effects (see Appendix A for details). Populations were measured in two sets of sub-areas of the map oriented parallel or at  $45^\circ$  to the faults, and ranging in size from  $A_1 = 1.75$  km to  $A_1 = 28$  km. Average population exponents (Fig. 3c) decrease gradually with diminishing scale for all three size measures ( $l$ ,  $u$  and  $m$ ). A comparison of the results for the two map orientations shows no discernable orientation bias. As in the EPC, the maximum throw population exponents are the most scale-sensitive (Fig. 2). Since all three population types are biased to some extent in the synthetic case (Fig. 3c), it is possible that the length populations are also biased in the EPC, but that the bias is not recognised due to the natural variability of the exponents (Fig. 2). In any case, this analysis shows that the observation of decreasing population exponent with decreasing scale observed for some size measures in EPC (Fig. 2) is not a function of non-power-law scaling, since qualitatively similar trends are observed in the fully-characterised synthetic system built with known assumptions (Fig. 3c). The remainder of this section aims to predict analytically trends in mean population exponent.

#### 3.3. Analytical method

In Table 2, we identify censoring geometries (A–E) which limit the size of a fault which is wholly or partially contained in the sample area of interest ( $A_1^2$ , Fig. 3a). For censoring type A, the fault is entirely contained in  $A_1^2$ , and  $s=S$ . For type B, one tip and  $T_{max}$  are in  $A_1^2$ . For type C, one tip is in  $A_1^2$  but  $T_{max}$  is not. For type D, both tips are outside  $A_1^2$  but  $T_{max}$  is in it. For type E, both tips as well as  $T_{max}$  are outside  $A_1^2$ . The censored geometry is a function of the relative sizes of  $L$  and  $A_1$ , and the position of the fault centre relative to the sample area (Fig. 4). Three size ranges must be considered; small faults with  $L \leq A_1$  (Fig. 4a), medium faults with  $A_1 < L \leq 2A_1$  (Fig. 4b) and large faults with  $2A_1 < L$  (Fig. 4c). The probabilities of sampling faults with each censoring type for each size range can be determined from the sizes of the shaded areas in Fig. 4, and are stated in Table 3 using the term  $p(L, A_1|X)$ , where X is censoring type (X = A, B, C, D or E).

The sampled sizes ( $s$ , where  $s = l$ ,  $u$  and  $m$ ) for each censoring type are functions of  $B$ ,  $n$ ,  $L$ ,  $A_1$  and  $L_x$  (Table 2). The length-term  $L_x$  is defined for each censoring type in Table 2, and depends on the location of the fault centre relative to the edges of  $A_1^2$ . When  $s$  depends on  $L_x$ , there is a range of possible censored outcomes, and therefore a probability of obtaining a particular outcome within



this range. This probability, which we term  $p(L \rightarrow s)$  (i.e. the probability that  $L$  is censored to  $s$ ) can be calculated using  $L_x$  (see Appendix B). In some cases,  $s$  does not depend on  $L_x$  (Table 2) and only one possible outcome exists which may or may not be censored and for which  $p(L \rightarrow s) = 1$ .

The total number of faults in  $A_1^2$  with sizes between  $s$  and  $s+ds$  can be determined from  $p(L, A_1 | X)$  and  $p(L \rightarrow s)$  using the expression:

$$n(s, A_1) = \sum_{X=A}^{X=E} \int_{\min L}^{\max L} n(L, A_0) p(L, A_1 | X) p(L \rightarrow s), \quad (8)$$

where the integral evaluates all cases for a censoring type and the summation considers all censoring types.  $n(L, A_0)$  is simply the total number of faults of total length  $L$  with centres in  $A_1^2$ , given by Eq. (3).

### 3.4. The maximum throw distribution

The probability that  $L$  is censored to  $u$ , required in Eq. (8), is (see Appendix B):

$$p(L \rightarrow u) = du / (BL^n), \quad \text{for } 0 < u \leq BL^n \text{ and } L_{\min} < L < 2A_1, \quad (9a)$$

$$p(L \rightarrow u) = du / (2A_1 BL^{n-1}), \quad \text{for } 0 < u \leq 2A_1 BL^{n-1} \text{ and } 2A_1 < L < L_{\max}, \quad (9b)$$


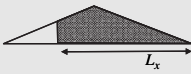

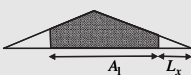

$$p(L \rightarrow u) = du / ((L - 2A_1)(BL^{n-1})), \quad \text{for } 2A_1 BL^{n-1} < u \leq BL^n \text{ and } 2A_1 < L < L_{\max} \quad (9c)$$

A graph (Fig. 5) can be constructed to determine the limits of integration and the limits of validity of  $u$  in  $n(u, A_1)$  (Eq. 8). Each shaded area in the plot represents a combination of: (a) censoring type, indicated by differences in shading; (b) uncensored fault size-range, indicated by values on the X axis; and (c) censored maximum throw size-range, indicated by values on the Y axis of Fig. 5. The limits of integration for Eq. (8) are either a constant ( $L=L_{\min}, A_1, 2A_1$  or  $L_{\max}$ ), or the equations  $L=(u/B)^{1/n}$  or  $L=(u/(2BA_1))^{1/(n-1)}$ . The limits of applicability of the resultant  $n(u, A_1)$  calculated with these limits are either the constant values of  $u$  labelled on the Y axis (Fig. 5), or the equations  $u=BL^n$  and  $u=2BA_1 L^{n-1}$  (Fig. 5). The arrowed portions of the relationship  $L=(u/B)^{1/n}$  represent the locations of censoring geometries A, B and D for which integration in Eq. (8) is not necessary since  $\min L = \max L = (u/B)^{1/n}$ .

Fig. 5 shows that Eq. (8) must be applied using five separate scale-ranges to evaluate the full scale-range of possible censored maximum throws ( $0 < u < BL_{\max}^n$ ). For example, consider a value of  $u$  in the scale-range  $BA_1^n < u < 2^n BA_1^n$  (Fig. 5). The total number of

**Fig. 3.** (a) An ideal power-law fault system is assumed to be present in a large square area of size  $A_0^2$  with faults equally oriented in two populations parallel to the edges of  $A_0$  and positioned randomly. Ideal fault populations are calculated for a smaller square area of size  $A_1^2$ . (b) Synthetic system of randomly positioned power-law sized faults. The thicker lines show the edges of sample areas (with edge length of  $A_1 = 28$  km) oriented parallel to each fault set and rotated  $45^\circ$  to them. (c) Mean, median and percentiles of length, maximum throw and geometric moment population exponents measured in sub-samples of the two areas highlighted in (b). The percentiles and the median values are for the set of sub-samples with edges parallel to the faults, and the set of measurements from the rotated samples are similarly variable. The labelled horizontal lines show the parent population exponents.

**Table 2**  
 Sampled length, maximum throw and geometric moment for the five censoring types as a function of the length term  $L_x$ . The fault is assumed to have a triangular throw profile, and the shaded regions indicate the portion of the fault sampled by each censoring type.

Censoring Type	Sampled Length ( $l$ )	Sampled Maximum Throw ( $u$ )	Sampled Geometric Moment ( $m$ )	
Type A		$L$	$BL^n$	$\frac{1}{2}BL^{n+1}$
Type B		$L_x$	$BL^n$	$2BL^n L_x + BL^{n-1} L_x^2 - \frac{1}{2}BL^{n+1}$
Type C		$L_x$	$2BL^{n-1} L_x$	$BL^{n-1} L_x^2$
Type D		$A_1$	$BL^n$	$2BL^n (A_1 + L_x) - BL^{n-1} (A_1 + L_x)^2 - \frac{1}{2}BL^{n+1}$
Type E		$A_1$	$2BL^{n-1} (L_x + A_1)$	$2BL^{n-1} A_1 L_x + BL^{n-1} A_1^2$

faults with sampled maximum throws in the range  $u$  to  $u + du$ , for any  $u$  in this range, is given from Eq. (8):

$$\begin{aligned}
 n(u, A_1) = & \int_{(u/B)^{1/n}}^{2A_1} (a_L A_0^2 L^{-c_L} dL) \left( \frac{LA_1}{A_0^2} \right) \left( \frac{du}{BL^n} \right) \\
 & + \int_{2A_1}^{L_{\max}} (a_L A_0^2 L^{-c_L} dL) \left( \frac{2A_1^2}{A_0^2} \right) \left( \frac{du}{2A_1 BL^{n-1}} \right) \\
 & + (a_L A_0^2 L^{-c_L} dL) \left( \frac{A_1^2}{A_0^2} \right) \quad (10)
 \end{aligned}$$

where the first and second terms (1 and 2 in Fig. 5) refer to medium sized faults ( $A_1 < L \leq 2A_1$ ) and large faults ( $2A_1 < L \leq L_{\max}$ ) subjected to censoring type C, and the third term (3 in Fig. 5) refers to faults subjected to censoring types B and D and for which  $p(L \rightarrow s) = 1$  and  $u = BL^n$  (Table 2).

Simplifying the first two terms, and integrating with respect to  $L$ , gives the number of faults in  $A_1^2$  which have a censored maximum throw in the range  $u$  to  $u + du$ :

$$\frac{a_L A_1 du}{B(2 - c_L - n)} \left[ L_{\max}^{2-c_L-n} - (u/B)^{(2-c_L-n)/n} \right].$$

The third term is expressed in terms of  $L$  and  $dL$ , rather than the desired  $u$  and  $du$ . Converting, we see that these faults have  $u = BL^n$  (Table 2), so  $L = (u/B)^{1/n}$  and  $dL = (du/nB)(u/B)^{(1-n)/n}$ . Replacing these relationships, we obtain the number of faults in  $A_1^2$  that have an uncensored maximum throw in the range  $u$  to  $u + du$ :

$$\frac{a_L A_1^2 (u/B)^{(1-c_L-n)/n} du}{Bn}.$$

Applying this method to all regions in Fig. 5, and simplifying, gives the frequency distribution of faults in  $A_1^2$  with

maximum throws in the range  $u$  to  $u+du$ , for the full range of  $u$ :

$$\begin{aligned}
 n(u, A_1) = & \frac{a_L A_1 du}{B(2 - c_L - n)} \left[ L_{\max}^{2-c_L-n} - L_{\min}^{2-c_L-n} \right] \\
 & \text{for } 0 < u \leq BL_{\min}^n \quad (11a)
 \end{aligned}$$

$$\begin{aligned}
 n(u, A_1) = & \frac{a_L A_1 du}{B(2 - c_L - n)} \left[ L_{\max}^{2-c_L-n} - (u/B)^{(2-c_L-n)/n} \right] \\
 & + \frac{a_L A_1^2 (u/B)^{(1-c_L-n)/n} du}{Bn} \\
 & \text{for } BL_{\min}^n < u \leq BL_{\max}^n \quad (11b)
 \end{aligned}$$

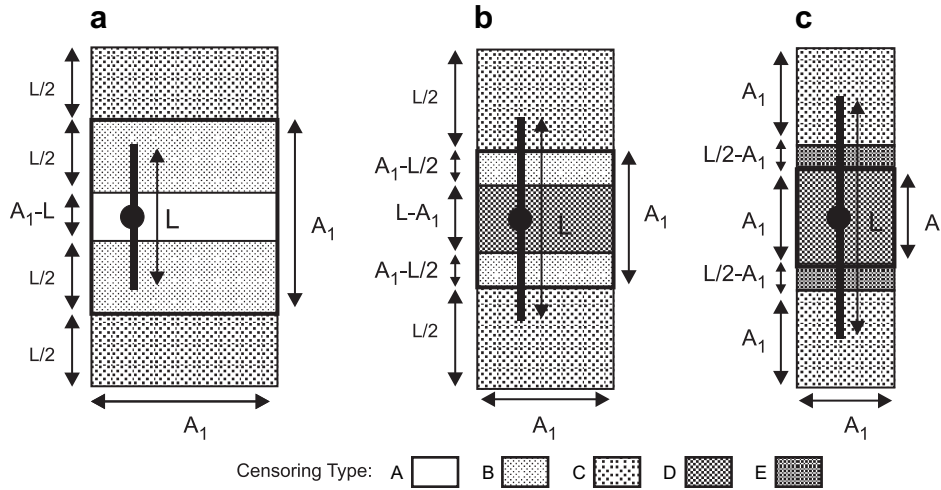
### 3.5. The trace length distribution

The censored length ( $l$ ) distribution can be determined in a similar manner to the censored maximum throw ( $u$ ) distribution (Eq. (11)). The main difference is that censoring types D and E censor faults to a maximum possible length,  $l = A_1$  (Table 2). For these faults,  $p(L \rightarrow s) = 1$ , and Eq. (8) simplifies to:

$$n(l = A_1, A_1) = \int_{A_1}^{L_{\max}} n(L, A_0) p(L, A_1 | D) + \int_{2A_1}^{L_{\max}} n(L, A_0) p(L, A_1 | E)$$

where  $n(l = A_1, A_1)$  is the number of faults of censored length  $A_1$  contained in  $A_1^2$ . Applying the full derivation gives the complete frequency distribution of faults in  $A_1^2$  with maximum lengths in the range  $l$  to  $l + dl$ :

$$n(l, A_1) = \frac{2a_L A_1 dl}{(1 - c_L)} \left[ L_{\max}^{1-c_L} - L_{\min}^{1-c_L} \right] \text{ for } 0 < l < L_{\min}. \quad (12a)$$



**Fig. 4.** Fault censoring type (see Table 2) as a function of the location of the fault centre within or adjacent to  $A_1^2$  and the relative sizes of  $L$  and  $A_1$ . The fault centre is shown as the dot on the example fault trace. (a)  $L \leq A_1$  (b)  $A_1 < L \leq 2A_1$ . (c)  $2A_1 < L$ . The illustrated geometries apply for both fault orientations.

$$n(l, A_1) = \frac{2a_L A_1 dl}{(1 - c_L)} [L_{\max}^{1-c_L} - l^{1-c_L}] + a_L A_1^2 l^{-c_L} dl - a_L A_1 l^{1-c_L} dl \quad \text{for } L_{\min} \leq l < A_1, \quad (12b)$$

$$n(l, A_1) = \frac{a_L A_1}{(2 - c_L)} [L_{\max}^{2-c_L} - A_1^{2-c_L}] - \frac{a_L A_1^2}{(1 - c_L)} [L_{\max}^{1-c_L} - A_1^{1-c_L}] \quad \text{for } l = A_1. \quad (12c)$$

$$\bar{N} = \frac{a_L A_1^2}{(1 - c_L)} (L_{\max}^{1-c_L} - L_{\min}^{1-c_L}) + \frac{a_L A_1}{(2 - c_L)} (L_{\max}^{2-c_L} - L_{\min}^{2-c_L}) \quad (13)$$

The probability density function of  $s$  in  $A_1^2$  ( $f(s)$ ) is, by definition,

$$f(s) = \frac{n(s, A_1)}{N ds} \quad (14)$$

**3.6. The geometric moment distribution**

The geometric moment ( $m$ ) distribution is considerably less amenable to an algebraic solution, and attempts to calculate  $p(L \rightarrow m)$  result in some intractable integrals. Therefore frequency distributions of  $m$  were determined numerically (see Appendix C for details). The procedure was checked by applying the same numerical method to determine the maximum throw distribution, and comparing this to the analytical distribution defined in Eq. (11).

**3.7. Probability density functions of fault size**

Integration of either Eq. (11) or (12) yields the expected total number of faults in  $A_1^2$ . We term this number  $\bar{N}$ , and it is:

**3.8. Distributions for the example synthetic map**

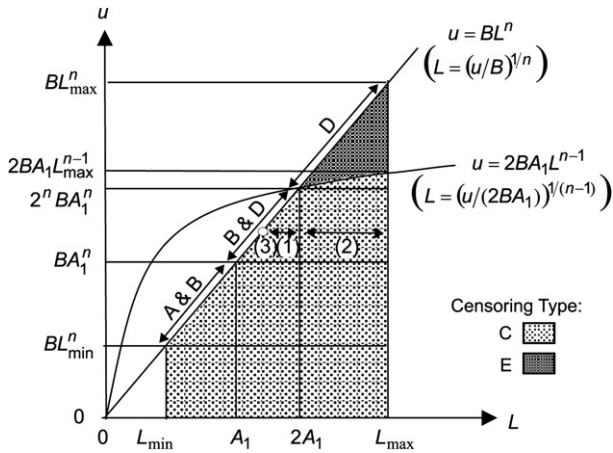
Analytically derived distributions for the synthetic system (Fig. 3b) are examined for sample sizes  $A_1 = 1.75$  km, 7 km and 28 km. Both the discrete and cumulative form of the distributions are shown (Fig. 6). The trace length pdfs (Fig. 6a) show an apparently stable power-law between  $L_{\min}$  and (a scale specific)  $l_{\max}$ , with an increased incidence of faults at  $l_{\max}$  reflecting those which completely cross the area ( $l_{\max} = A_1$ ; Eq. 12c). A close examination is needed to show that the distribution is not a perfect power-law, as the local exponent varies only slightly over the length-scales covered by the distribution (Fig. 6d). The maximum throw and moment pdfs (Fig. 6b,c) are more obviously non-power-law, and the local power-law exponents of these distributions tend towards infinity as the fault size tends towards the (vanishingly unlikely) largest possible size.

**Table 3**

Conditional probability  $p(L, A_1 | X)$  that a fault of length  $L$  is sampled in  $A_1^2$  subject to each censoring type ( $X = A-E$ ), and the minimum and maximum possible values of  $L_x$  (see Table 2) associated with each censoring type, for small ( $L_{\min} \leq L \leq A_1$ ), medium ( $A_1 \leq L \leq 2A_1$ ) and large ( $L \geq 2A_1$ ) faults.

Censoring Type	$L_{\min} \leq L \leq A_1$			$A_1 < L < 2A_1$			$2A_1 < L < L_{\max}$		
	$p(L, A_1   X)$	$L_{x_{\min}}$	$L_{x_{\max}}$	$p(L, A_1   X)$	$L_{x_{\min}}$	$L_{x_{\max}}$	$p(L, A_1   X)$	$L_{x_{\min}}$	$L_{x_{\max}}$
Type A	$\frac{(A_1^2 - LA_1)}{A_0^2}$	-	-	0	-	-	0	-	-
Type B	$\frac{LA_1}{A_0^2}$	$\frac{L}{2}$	$L$	$\frac{(2A_1^2 - LA_1)}{A_0^2}$	$\frac{L}{2}$	$A_1$	0	-	-
Type C	$\frac{LA_1}{A_0^2}$	0	$\frac{L}{2}$	$\frac{LA_1}{A_0^2}$	0	$\frac{L}{2}$	$\frac{2A_1^2}{A_0^2}$	0	$A_1$
Type D	0	-	-	$\frac{(LA_1 - A_1^2)}{A_0^2}$	0	$\frac{(L - A_1)}{2}$	$\frac{A_1^2}{A_0^2}$	$\frac{(L - 2A_1)}{2}$	$\frac{(L - A_1)}{2}$
Type E	0	-	-	0	-	-	$\frac{(LA_1 - 2A_1^2)}{A_0^2}$	0	$\frac{(L - 2A_1)}{2}$





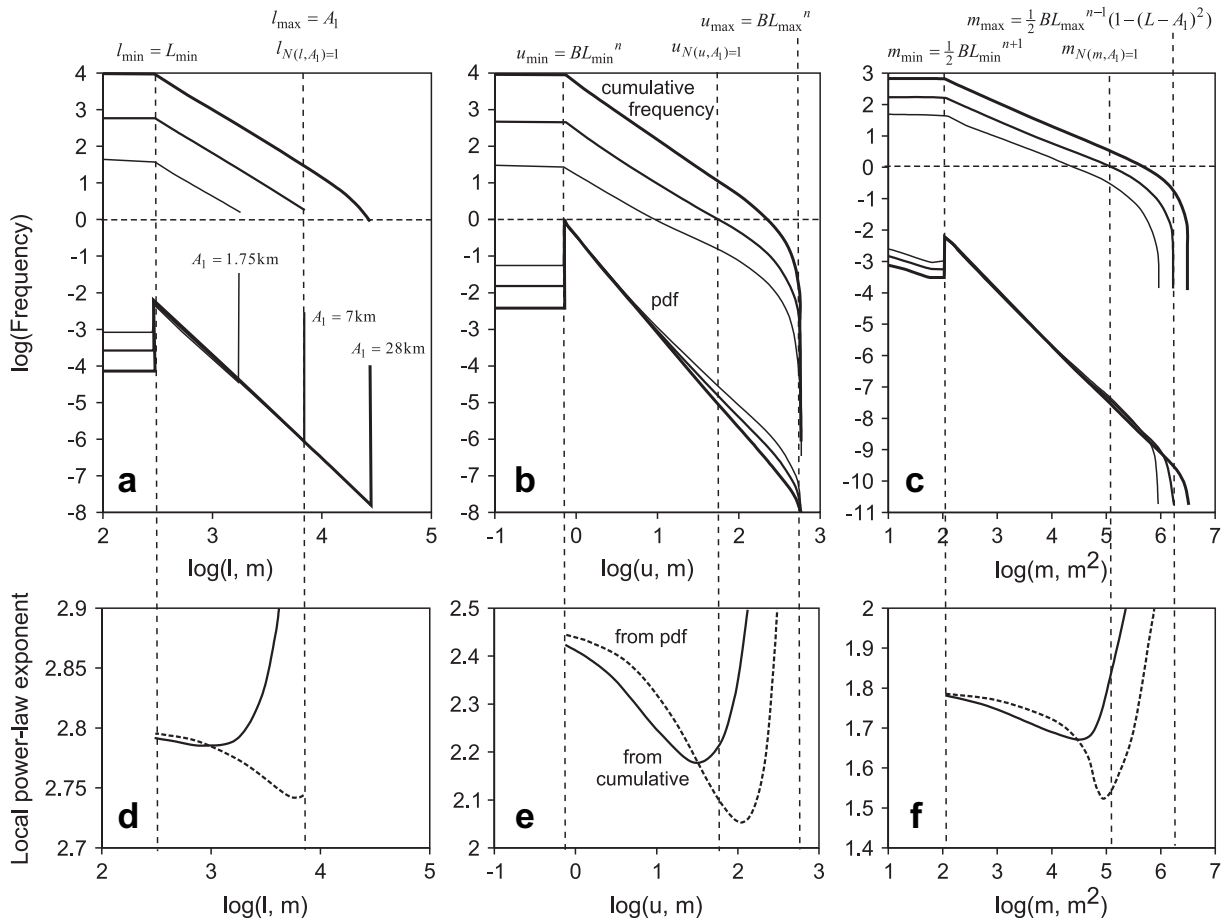
**Fig. 5.** Graphical determination of the limits of integration of Eq. (8) when applied to maximum throw. Lines (1) and (2), and point (3), show the total fault lengths which give rise to a fault with a censored size  $u$  in the range  $BA_1^n < u < 2^n BA_1^n$ . See text for discussion.

Different best-fit power-law exponents would be inferred for the three population types depending on which form of the distribution (discrete or cumulative) is used, and the size interval

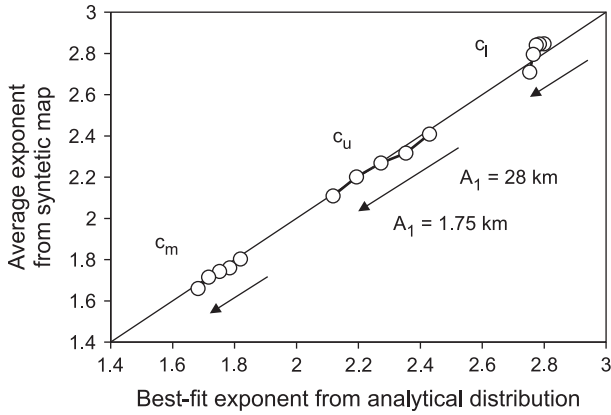
from which it is estimated (Fig. 6d–f). A representative sample of the system is unlikely to contain any faults larger than  $S_{N(s,A_1)=1}$ , the size corresponding to a cumulative frequency of 1 (Fig. 6), but is likely to contain smaller faults. Therefore the most representative range for estimating power-law exponents is  $S_{\min} < s < S_{N(s,A_1)=1}$ . This range is highlighted for the case  $A_1 = 7$  km in Fig. 6. The exponent can be estimated more reliably when the distribution is less variable. For the trace length population,  $c_l$  estimated from the discrete distribution is less variable over the representative scale-range (e.g. Fig. 6d), while  $c_u$  and  $c_m$  are less variable if they are estimated from the cumulative form of the distribution (Fig. 6e,f).

The estimated exponents derived from the analytical treatment (using linear regression of the least variable form of the distribution over the representative range) match well the average exponents measured in the synthetic map for  $c_u$  and  $c_m$ , but are less accurate for  $c_l$  (Fig. 7). We ascribe this poorer match for  $c_l$  to a combination of a lower susceptibility of  $c_l$  to scaling bias, which was observed in Fig. 3c for the synthetic map as well as predicted from the pdfs, and of a greater natural variability in value (Fig. 3c), resulting in a greater uncertainty on the measured mean value.

The good overall match between predicted scale-specific  $c_s$  and that measured in the synthetic map validates the analytical method for determining the scale-specific population exponents (Fig. 7). The results therefore permit estimation of scaling biases over



**Fig. 6.** (a) Analytically derived censored length,  $l$ ; (b) maximum throw,  $u$ ; and (c) geometric moment,  $m$  distributions for sub-areas with  $A_1 = 28$  km (thickest lines), 7 km and 1.75 km (thinnest lines). The three upper sets of curves show the cumulative frequency distributions and the lower curves show the pdfs. The dashed horizontal lines (at  $N(s,A_1) = 1$ ) intersect the cumulative frequency distributions at the largest expected fault in a representative sample (i.e. at  $S_{N(s,A_1)=1}$ ). (d–f) The local exponents for the samples with  $A_1 = 7$  km derived from the cumulative frequency distributions (solid lines) and the pdfs (dashed lines). The dashed vertical lines (a–f) are specific to the distributions for  $A_1 = 7$  km, and show the ranges over which the representative exponent is determined ( $S_{\min} < s < S_{N(s,A_1)=1}$ ), and the largest possible sampled fault ( $S_{\max}$ ).



**Fig. 7.** Comparison between the best-fit exponents from the analytical distributions (i.e. Fig. 6, and equivalent for scales not shown in Fig. 6) and the mean values of the measured populations in the synthetic map (i.e. Fig. 3c). The arrows indicate the effect of decreasing sample size from 28 km to 1.75 km in each population type.

a range of possible map samples without needing to measure population exponents in many sub-areas of many synthetic maps.

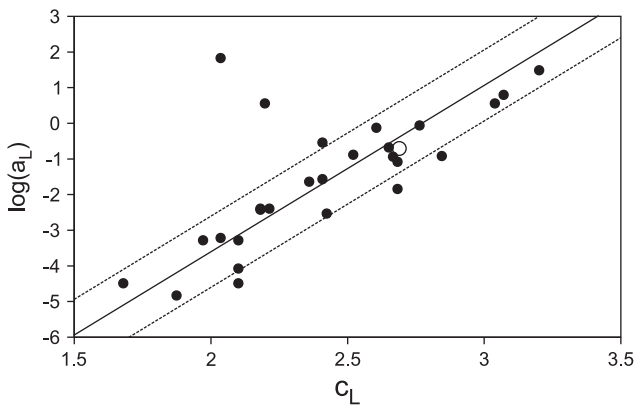
### 3.9 General trends in fault population scaling biases

The length population depends on  $a_L$ ,  $c_L$ ,  $A_1$ ,  $L_{max}$ ,  $L_{min}$  (Eq. 12), and all these variables potentially influence bias in the fault-trace length power-law exponent ( $c_l$ ). The maximum throw and geometric moment populations depend additionally on  $B$  and  $n$  (e.g. Eq. (11)), but  $B$  is found not to influence population bias.

It is appropriate when generalising effects to consider representative values of variables first, and it is convenient to consider the length terms as ratios. The ratio between the smallest adequately sampled fault-trace length ( $L_{min}$ ) and the edge of the map ( $A_1$ ) relates to resolution, and the compilation of Bonnet et al. (2001) shows that published population exponents derive from samples for which this ratio ranges from 1/3 to 1/200, and have a median value of 1/30. Parameters  $a_L$  and  $c_L$  are approximately linked (with a couple of outliers) for fault systems by the relationship (Fig. 8):

$$a_L \approx 10^{4.67c_L - 12.933} \quad (15)$$

An approximate link between these parameters is not surprising since  $a_L$  must change if  $c_L$  is changed while fault density is held



**Fig. 8.** Compilation of  $a_L$  vs.  $c_L$  for fault maps (● are data compiled by Bonnet et al., 2001; ○ is the most likely case for the EPC from this paper). The solid line shows the representative trend (Eq. (15)), and the dashed lines are for systems with one order of magnitude more or less faults than this case.

constant (e.g. Westaway, 1994), and the form of the change will depend on the precise definition of fault density. Values of  $n$  measured from natural faults range from about 0.5 to 1.5 (e.g. Gillespie et al., 1992; Schultz et al., 2008), and a value of  $n = 1$  is representative of many systems.

Fault-trace map samples with  $L_{min}/A_1=1/30$ ,  $n = 1$ , and with  $a_L$  and  $c_L$  linked by Eq. (15), are therefore representative of those reported in the literature. Fault population scaling bias for these representative samples, as a function of the remaining variables ( $c_S$  and the ratio  $A_1/L_{max}$ ), are shown in Fig. 9a–c. Bias is usually  $<0.1$  for the length and moment populations, but can be up to about 0.35 for  $u$ .

Fig. 9d–f examines the biases as a function variables kept constant in Fig. 9a–c, for systems with  $c_L=2.5$ ,  $L_{max}/A_1 = 100$  and  $n = 1$ . The axes of Fig. 9d–f are the ratio  $L_{min}/A_1$ , and a multiplier of  $a_L$  spanning the range indicated in Fig. 8. Bias is greater for lower resolution (i.e. higher  $L_{min}/A_1$ ) or denser (i.e. higher  $a_L$ ) systems, and reaches a maximum for the  $l$  populations once  $a_L$  is sufficiently large so that at least one fault with  $l = A_1$  can be expected. Since  $u_{max}$  and  $m_{max}$  are unbound (Fig. 6), no limit to the trend for bias as a function of  $a_L$  exists in these populations (Fig. 9e, f). Effects on bias of the final variable ( $n$ ; shown for completeness in Fig. 9g, h) are smaller for characteristic systems than the other system variables.

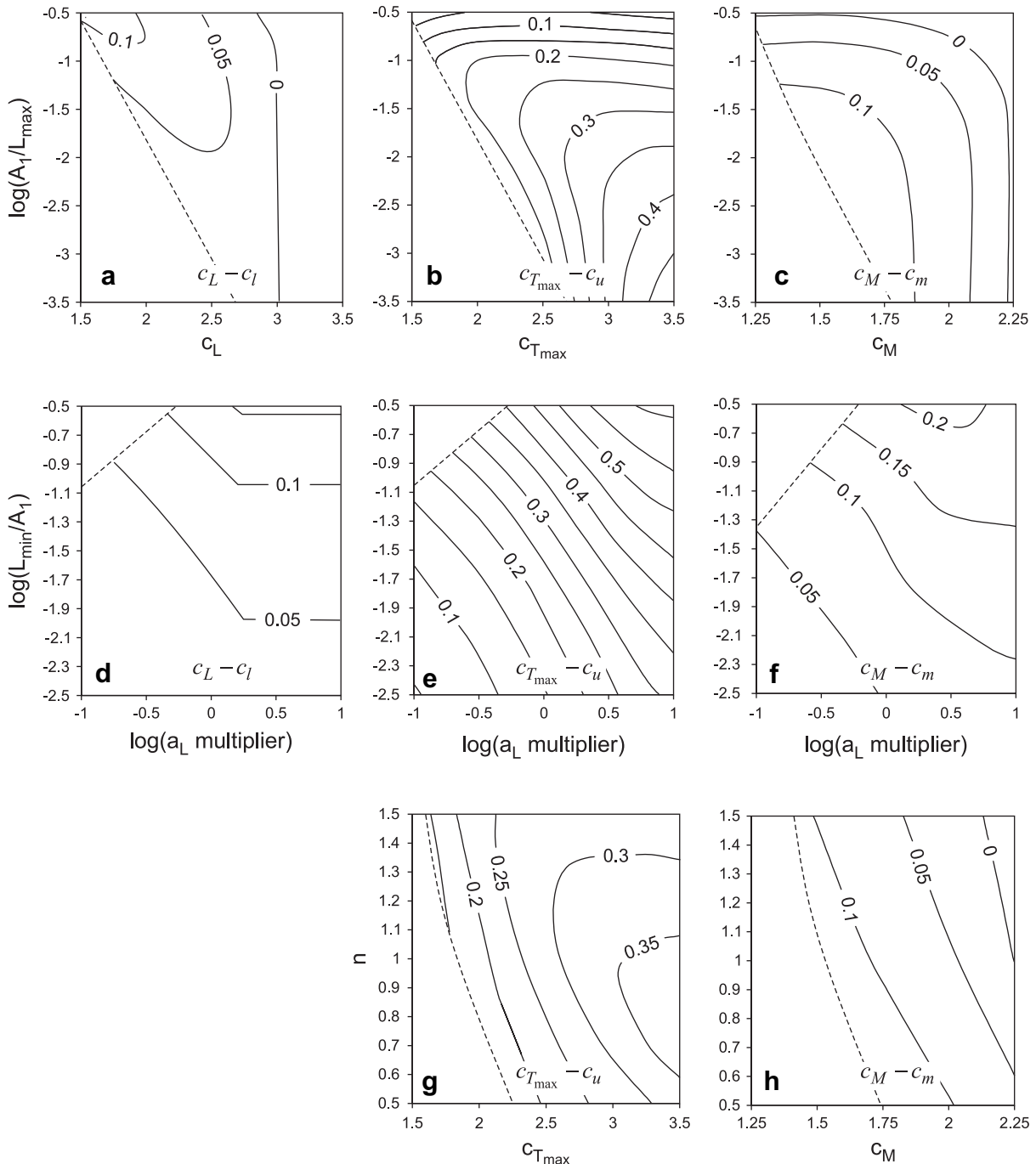
These results (Fig. 9) indicate that scaling biases can be significant for maximum throw and to a lesser extent geometric moment populations. For trace-length, a bias  $>0.1$  is only likely in unusual systems. The biases have complex dependencies and we have mapped out some of these dependencies in Fig. 9, but the expected bias in any particular  $u$  or  $l$  population can be assessed directly by evaluating the pdfs (Eqs. (11) and (12)). The maximum throw population is approximately three times as prone to bias than the length or moment populations. Of particular note is the tendency for samples of greater density fault systems to be more biased than samples of lesser density ones. These samples will contain more data and might therefore be considered more reliable. However, although estimation bias might be smaller for such samples, scaling bias will be greater.

### 4. Application to the East Pennines Coalfield faults

The analytical results are tested for a natural system using the East Pennines coal-field fault populations (Figs. 1 and 2). A maximum likelihood estimation (MLE) method is used to estimate the unbiased parent population using the six samples with  $A_1 = 10$  km, and the observed populations in the smaller areas ( $A_1 = 2.5$  and 5 km) are then tested against the scale-specific predictions deduced from this maximum likelihood parent population. The test is considered successful if the mean observed scale-specific exponents (Fig. 2) are predicted to within a small fraction of their variability.

The MLE method calculates the probability that a set of observations (in this case the populations measured in areas with  $A_1 = 10$  km; Fig. 10) are the outcome of a particular input condition (in this case a parent fault system characterised by particular values of  $c_L$ ,  $a_L$ ,  $B$ ,  $n$ ,  $L_{max}$  and  $L_{min}$ ). The method relies on evaluating the probability for different input conditions, and identifying the condition that yields the greatest probability. This condition is said to be the maximum likelihood estimate.

Our analysis uses four summary properties for each sample to evaluate the probability of the sample deriving from a particular parent population. These properties are the exponents of the trace length and maximum throw populations ( $c_l$  and  $c_u$ ), the number of faults longer than 2 km in the sample ( $N(l \geq 2 \text{ km}, A_1)$ ), and the number of faults with maximum throws larger than 10 m in the sample ( $N(u \geq 10 \text{ m}, A_1)$ ). These sizes (2 km length and 10 m throw) are used as they are close to the centre of the total range of fault sizes (Fig. 10). Hence  $N(l \geq 2 \text{ km}, A_1)$  and  $N(u \geq 10 \text{ m}, A_1)$  are unlikely



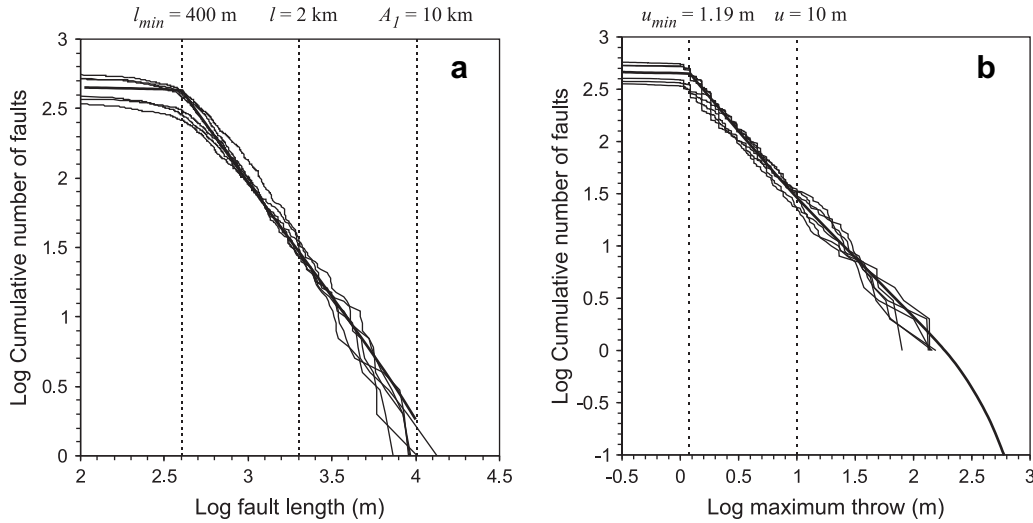
**Fig. 9.** Predicted scaling bias ( $c_s - \bar{c}_s$ ) for systems of randomly distributed power-law sized faults. Bias in (a) fault-trace length, (b) maximum throw and (c) geometric moment populations for representative systems ( $L_{\min}/A_1 = 1/30$ ,  $n = 1$ ,  $a_L$  given by Eq. (15)) as a function of sample scale ( $A_1/L_{\max}$ ) and unbiased exponent ( $c_s$ ). (d–f) Bias as a function of sample resolution ( $L_{\min}/A_1$ ) and  $a_L$ , for systems with  $A_1/L_{\max} = 1/100$ ,  $n = 1$  and  $c_L = 2.5$  (d),  $c_{T_{\max}} = 2.5$  (e) or  $c_M = 1.75$  (f). (g–h) Bias as a function of  $n$  and  $c_s$  for systems with  $L_{\min}/A_1 = 1/30$ ,  $A_1/L_{\max} = 1/100$ , and  $a_L$  given by Eq. (15). See text for discussion.

to be affected by truncation bias, but are still large enough to be representative of the fault populations (they average about 30 faults). The analysis assumes throughout that  $L_{\min} = 400$  m.

Each input condition to be tested (an assumed parent population) is characterised by an ideal distribution at the scale of interest (e.g. Fig. 6), with ideal exponents ( $\bar{c}_s$ ), and with ideal expected numbers of faults larger than particular sizes ( $\bar{N}(s, A_1)$ ). A random sample of the distribution will have values of  $c_s$  and  $N(s, A_1)$  which will generally not be the same as the ideal expectations. The distribution of  $c_s$  around  $\bar{c}_s$ , and of  $N(s, A_1)$  around  $\bar{N}(s, A_1)$ , are

required for calculating the probability that a sample derives from the parent system. Exponent  $c_s$  follows a normal distribution, characterised by a mean ( $\bar{c}_s$ ) and a standard deviation ( $\sigma_{c_s}$ ), while  $N(s, A_1)$  follows a Poisson distribution, which is a function only of  $\bar{N}(s, A_1)$ . Details of the two distributions are given in Appendix D.

Each of the six EPC areas with  $A_1 = 10$  km has particular values of  $c_l$ ,  $c_u$ ,  $N(l \geq 2 \text{ km}, A_1)$  and  $N(u \geq 10 \text{ m}, A_1)$ . The probability that any one of the measured exponents derives from an assumed parent population is termed  $p(c_{s_x})$  where  $c_{s_x}$  is the exponent for sample  $x$ , and is calculated by subtracting the cumulative probability value at



**Fig. 10.** Cumulative frequency populations for (a) length and (b) maximum throw, for the six 10 km sample areas of the East Pennines Coalfield fault map (thin lines). The thicker lines show the maximum likelihood case sampled to this scale. The dashed vertical lines show the minimum fault sizes assumed in the analysis and the sizes ( $l = 2 \text{ km}$ ,  $u = 10 \text{ m}$ ) used to constrain the solution. See text for discussion.

$c_{s_x} - 0.05$  from the cumulative probability value at  $c_{s_x} + 0.05$  (these cumulative probabilities are calculated from  $\bar{c}_s$  and  $\sigma_{c_s}$ ). The probability that  $N(s, A_1)_x$  (the measured number of faults for sample  $x$ ) derived from an assumed parent population is termed  $p(N(s, A_1)_x)$ , and is determined from  $\bar{N}(s, A_1)$  using the Poisson distribution. The probability that all six samples derive from the particular parent system considered is the product of 24 individual probabilities:

$$p(\text{Parent}) = \prod_{x=1}^{x=6} p(c_{l_x})p(c_{u_x})p(N(l \geq 2 \text{ km}, A_1)_x) \times p(N(u \geq 10\text{m}, A_1)_x) \quad (16)$$

The choice of range around  $c_{s_x}$  used to calculate  $p(c_{s_x})$  (i.e.  $c_{s_x} \pm 0.05$ ) is arbitrary, and a greater range would give higher values of  $p(\text{Parent})$ . Hence the precise values of  $p(\text{Parent})$  obtained from Eq. (16) are unimportant; instead the relative probabilities, which are unaffected by the range used for  $c_{s_x}$ , are what is significant.

Fig. 11 shows contours of  $p(\text{Parent})$  normalised by the maximum  $p(\text{Parent})$  value obtained. There is an equally probable maximum likelihood solution for any value of  $L_{\text{max}}$ , but, provided  $L_{\text{max}}$  is a few times larger than  $A_1$ , the maximum likelihood values of  $c_L$ ,  $a_L$ ,  $B$  and  $n$  do not change. Hence the maximum likelihood estimation shown in Fig. 11, which assumes that  $L_{\text{max}} = 10A_1$ , is essentially independent of  $L_{\text{max}}$ . This MLE solution implies that the unbiased EPC population is characterised by  $c_L = 2.685$ ,  $a_L = 0.174$ ,  $B = 0.00083$ ,  $n = 1.213$ .

The applicability of the analytical results to the natural system are tested by predicting the biased exponents in different sized sample areas of the EPC ( $A_1 = 2.5$  and  $5 \text{ km}$ ) based on the MLE solution, and comparing them to the measured exponents (Fig. 2). This test, shown in Fig. 12, indicates a close match between obtained and predicted exponents for the  $c_l$  and  $c_m$  populations. The prediction is a less accurate reflection of the mean measured length population exponents ( $c_l$ ), since the analytical results predict a slight scaling bias that could not be recognised, but is probably present, in the initial measurements (Fig. 2). However, the maximum discrepancy between measured and predicted  $c_l$  is only a small fraction (ca. 12%) of the standard deviation of the measured (or predicted using Eq. (D2)) exponent. Hence, despite these discrepancies in mean value of length exponent, the test is a success and both the analytical results, and the MLE solution, are appropriate for the East Pennine coal-field fault system.

### 5. Conclusions

Power-law exponents for populations of different measures of fault size show different trends with respect to map sample scale in the East Pennines Coalfield fault system. Maximum throw populations and geometric moment populations have mean exponents that decrease systematically with decreasing scale. Fault-trace length population exponents are more naturally variable and are not demonstrably scale-dependent.

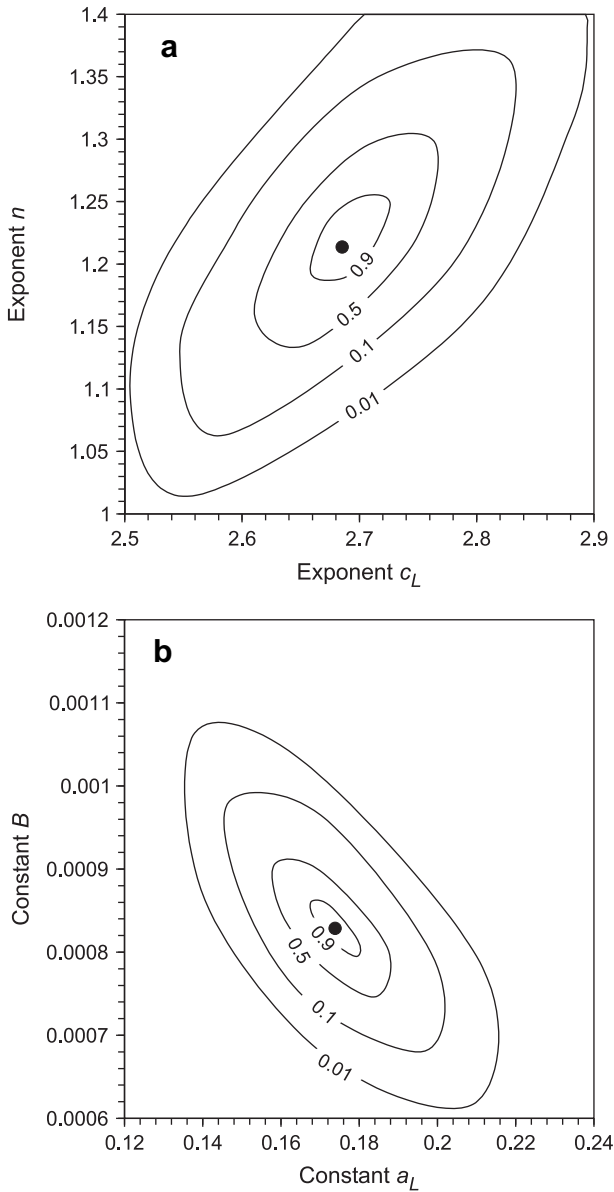
Similar trends are present in a synthetic map with known fault scaling characteristics and random fault locations, and are caused by sampling bias. Size bias and censoring bias have opposing effects, and for fault-trace length populations the two biases appear to approximately cancel out. For the other population types, the trends are attributed to a progressive dominance of size bias over censoring bias in progressively smaller map samples. Orientation bias is negligible in the orthogonal systems considered.

The scaling biases are rationalised by examining analytically derived expected length, maximum throw and geometric moment distributions of areal sub-samples of a fault system with randomly distributed fault locations and power-law fault sizes. Although strictly non-power-law, the size distributions can be approximated to power-law distributions with scale-specific exponents. The best-fit exponents of the analytically derived expected fault size distributions match closely the average exponents measured in the synthetic fault map at the same scales.

The results are generalised in Fig. 9, which records bias in the expected population exponents for the different population types as a function of map scale, resolution, and the characteristics of the unbiased fault system. Population exponents deduced from fault maps representative of many of those published are unlikely to be biased by more than 0.1 for the length population, but scaling biases of 0.3 or more are likely for maximum throw populations. These conclusions are derived from analysis of idealised systems of randomly-positioned faults with negligible orientation bias, and power-law exponents in anisotropic and/or clustered fault systems may scale differently.

The results are applicable to the East Pennines Coalfield fault system where they have been used to estimate the unbiased parent population based on six  $100 \text{ km}^2$  sub-samples. The population exponents in  $6.25$  and  $25 \text{ km}^2$  sub-samples predicted from this estimate match well the means of the measured values at these scales.





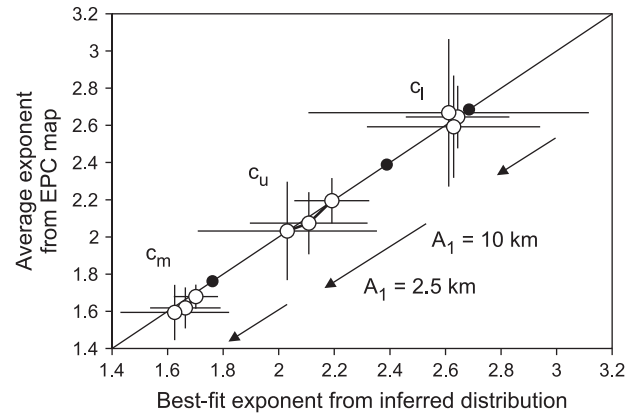
**Fig. 11.** Contours of the relative probability of a parent population having values of  $n$ ,  $c_L$ ,  $a_L$  and  $B$ , assuming  $L_{\max} = 10A_1$ . Contours in (a) reflect the local maximum probability case of  $a_L$  at each combination of  $c_L$  and  $n$  (these probabilities are independent of  $B$ ). Contours in (b) assume  $c_L = 2.685$ ,  $n = 1.213$  (i.e. the most likely case in (a)). The dots indicate the maximum likelihood combination of the four variables.

### Acknowledgements

We are grateful for comments from reviewer M. Mauldon and editor W.M. Dunne which have enabled us to improve our presentation.

### Appendix A

The synthetic map (Fig 3b) is of a system with  $A_0 = 40$  km,  $a_L = 0.5878$ ,  $c_L = 2.80$ ,  $B = 0.000676$ ,  $n = 1.226$ ,  $L_{\max} = 69722$  m and  $L_{\min} = 300$  m. Edge effects were considered in its construction as follows: Eq. (3) gives the number of faults of length  $L$  with centres in the area  $A_0^2$ , but does not include those faults with centres outside  $A_0^2$ , which have some of their length in the area. The centre of a fault of length  $L$ , positioned anywhere in a rectangular area of size  $A_0(A_0 + L)$  centred



**Fig. 12.** Comparison between the scale specific best-fit exponents deduced analytically from the maximum likelihood estimate of the parent population in the EPC, and the averages of the measured populations in the EPC map. The arrows indicate the effect of decreasing sample size from 10 km to 2.5 km in each population type. The black dots show the estimated parent population exponents. The error bars reflect one standard deviation of either the measured variability (Y-error bars, see Fig. 2) or the variability predicted from Eq. (D2) (X-error bars).

on the area  $A_0^2$ , will be partially or completely sampled in  $A_0^2$  (e.g. Fig. 4). Therefore the number of faults sampled in  $A_0^2$ , irrespective of whether the fault centre is in the area or not, is given by:

$$n'(L, A_0) = a_L A_0 (A_0 + L) L^{-c_L} dL, \quad (A1)$$

where  $n'(L, A_0)$  is the number of faults with uncensored lengths in the range  $L$  to  $L + dL$  which are at least partially sampled in the area of interest  $A_0^2$ . The Inverse Transform method (e.g. Pickering et al., 1995) is applied to the integral of Eq. (A1) to give an uncensored trace length population. Each fault in this population is assigned to one of the two orientation directions at random, and the centre-point of the fault is then chosen as a random location within the orientation- and length- dependent rectangular area  $A_0(A_0 + L)$ . This method minimises the number of faults which need to be placed, while ensuring that the map of interest does not have any edge effects.

### Appendix B

The probable value of  $L_x$  is distributed uniformly between the values of  $L_{x_{\min}}$  and  $L_{x_{\max}}$  reported in Table 3. A uniform distribution of  $L_x$  arises because an equal probability exists that the centre of a fault sampled by a particular censoring type lies anywhere in the relevant sampling area (Fig. 4). The pdf of  $L_x$  is therefore:

$$f(L_x) = \left( \frac{1}{L_{x_{\max}} - L_{x_{\min}}} \right) \quad \text{for } L_{x_{\min}} \leq L_x \leq L_{x_{\max}}. \quad (B1)$$

The pdf of censored fault size ( $f(s)$ ) can be derived from  $f(L_x)$  using the standard method of transformations (e.g. Mendenhall et al., 1986), whereby

$$f(s) = f(L_x) \left| \frac{dL_x}{ds} \right|. \quad (B2)$$

The probability of obtaining a censored fault in the size range  $s$  to  $s + ds$  (i.e.  $p(L \rightarrow s)$ ) derives directly from  $f(s)$ :

$$p(L \rightarrow s) = \int_s^{s+ds} f(s) ds. \quad (B3)$$

$dL_x/ds$  (Eq. B2) is obtained within the limits of validity of  $L_x$  listed in Table 3 by restating the equations given in Table 2 as a function of  $L_x$  and differentiating. For example, consider the censored maximum fault throw (i.e.  $s = u$ ), for faults of size  $A_1 < L \leq 2A_1$ , subject to censoring type C. For these faults we have  $u = 2BL^{n-1}L_x$  for  $0 < L_x \leq L/2$ , therefore  $L_x = u/(2BL^{n-1})$  for  $0 < u \leq BL^n$ . Differentiating, we obtain  $dL_x/du = 1/(2BL^{n-1})$ . Replacing these in Eqs. (B1) and (B2) gives  $f(u) = 1/(BL^n)$  for  $0 < u \leq BL^n$  and  $A_1 < L \leq 2A_1$ . From this it follows (Eq. (B3)) that  $p(L \rightarrow s) = du/(BL^n)$ , for the same limits of  $u$  and  $L$ .

For censoring type C at all three scales and for censoring type E for the largest scale,  $u$  is a function of  $L_x$  (Tables 2 and 3). Applying the approach of Eq. (B3) to these four cases, we obtain probabilities given in Eq. (9). Note that Eq. (9a) derives from censoring type C for both small and medium faults, as both the expression and limits of  $f(u)$  are the same for these faults. Note also that the sampled maximum throws of faults subjected to censoring types A, B and D do not depend on  $L_x$  (Table 2), and for these faults  $u = BL^n$  and  $p(L \rightarrow s) = 1$ .

### Appendix C

The numerical solution to Equation (8) for geometric moments is based on the trapezium rule for integration and takes the following steps:

- Step 1. Choose a value of  $m$  for which to evaluate  $N(m, A_1)$ , and use a constant value of  $dm$  for all values of  $m$ .
- Step 2. Choose a length in the range  $L_{min} < L < L_{max}$ , incrementing by a small value ( $dL$ ) each time this step is repeated.
- Step 3. Calculate the probable number of faults with lengths in the range  $L$  to  $L + dL$  and with centres contained in  $A_0^2$  (i.e.  $N(L, A_0)$ ; Eq. (3)).
- Step 4. For censoring type B to E determine  $p(L, A_1|X)$ . These probabilities are given in Table 3.
- Step 5. For the value of  $L$  being considered, and for each censoring type for which  $p(L, A_1|X) > 0$ , there is one possible range of  $L_x$  that can give rise to the target  $m$  in the range  $m$  to  $m + dm$ . (Table 2). The probability of obtaining  $L_x$  in this range (i.e.  $p(L \rightarrow m)$ ) is determined from the uniform distribution of  $L_x$  (Eq. (B1), Table 3).
- Step 6. The product of  $N(L, A_0)$ ,  $p(L, A_1|X)$  and  $p(L \rightarrow m)$  (Steps 3–5), summed for each possible censoring type, is the total number of faults with  $m$  in the range  $m$  to  $m + dm$  deriving from the value of  $L$  in question.
- Step 7. Repeat Steps 2–6 for all values of  $L$ , to obtain the total number of faults of size  $m$  in  $A_1$  deriving from all possible values of  $L$ . (i.e.  $N(m, A_1)$ ).
- Step 8: Repeat Steps 1–7 for the full range of  $m$  to obtain the full distribution of  $N(m, A_1)$ .

Censoring type A is not included in this numerical treatment, because  $N(m, A_1)$  deriving from censoring type A can be determined analytically, and then simply added to the value of  $N(m, A_1)$  determined numerically for the other censoring types using the steps outlined above.

### Appendix D

The distribution of  $N(s, A_1)$  around  $\bar{N}(s, A_1)$  is characterised by the Poisson distribution:

$$p(N(s, A_1)) = \frac{e^{-\bar{N}(s, A_1)} \bar{N}(s, A_1)^{N(s, A_1)}}{N(s, A_1)!} \quad (D1)$$

where  $p(N(s, A_1))$  is the probability that the sample contains exactly  $N(s, A_1)$  faults given that the expected number of faults is  $\bar{N}(s, A_1)$ . A Poisson distribution is appropriate given the assumption that fault centres are randomly located.

The distribution of  $c_s$  around  $\bar{c}_s$  is described with a general expression derived from Monte Carlo simulation. Many thousands of samples of trace length or maximum throw populations were drawn from various distributions, with the number of faults in the sample selected using a Poisson distribution (Eq. (13) defines the total expected number,  $\bar{N}$ ), and their sizes drawn from the analytically derived pdfs (Eq. (14)). For each sample, the population slope ( $c_s$ ) was estimated using a log-frequency plot and the distribution in  $c_s$  for all samples was analysed as a function of the variables defining the input size distribution. Overall,  $c_s$  was found to be approximately normally distributed with a mean slope equal to the expected slope ( $\bar{c}_s$ ) and with a standard deviation ( $\sigma_{c_s}$ ) that approximates:

$$\sigma_{c_s} \approx 1.32(\bar{c}_s - 1)\bar{N}^{-0.4}, \quad (D2)$$

where  $\bar{N}$  is the expected number of faults in the sample.

This empirically derived expression matches the measured variability in the population slopes of the synthetic map (Fig. 3) as well as those measured in other Monte Carlo simulations covering a wider range of  $\bar{N}$  and  $\bar{c}_s$ . It predicts slightly greater values of ( $\sigma_{c_s}$ ) than the equivalent expression derived by Pickering et al. (1995), and this result must be in part because we include variations in  $N$  in our Monte Carlo simulations through use of the Poisson distribution, but may also be a consequence of a different implementation of the log-interval method (i.e. the sizes of the bins and amount of overlap between them).

### References

- Ackermann, R.V., Schlichte, R.W., Withjack, M.O., 2001. The geometric and statistical evolution of normal fault systems: an experimental study of the effects of mechanical layer thickness on scaling laws. *Journal of Structural Geology* 23, 1803–1819.
- Bailey, W.R., Manzocchi, T., Walsh, J.J., Keogh, K., Hodgetts, D., Rippon, J., Nell, P.A.R., Flint, S., Strand, J.A., 2002. The effect of faults on the 3-D connectivity of reservoir bodies: a case study from the East Pennine Coalfield, U.K. *Petroleum Geoscience* 8, 263–277.
- Bailey, W.R., Walsh, J.J., Manzocchi, T., 2005. Fault populations, strain distribution and basement reactivation in the East Pennines Coalfield, U.K. *Journal of Structural Geology* 27, 913–928.
- Barr, D., 2007. Conductive faults and sealing fractures in the West Sole gas fields, southern North Sea. In: Jolley, S.J., Barr, D., Walsh, J.J., Knipe, R.J. (Eds.), *Structurally Complex Reservoirs*. Geological Society, London, Special Publications, vol. 292, pp. 431–452.
- Belfield, W.C., 1992. Simulation of subseismic faults using fractal and multifractal geometry (SPE paper 24751). *Proceeding of the 67th SPE Annual Technical conference and Exhibition*, October 5–7, 1992, Washington DC, USA, pp. 903–911.
- Berkowitz, B., Bour, O., Davy, P., Odling, N.E., 2000. Scaling of fracture connectivity in geological formations. *Geophysical Research Letters* 27, 2061–2064.
- Bonnet, E., Bour, O., Odling, N.E., Davy, P., Main, I., Cowie, P., Berkowitz, B., 2001. Scaling of fracture systems in geological media. *Reviews of Geophysics* 39, 347–383.
- Clark, R.M., Cox, S.J.D., Laslett, G.M., 1999. Generalization of power-law distributions applicable to sampled fault-trace lengths: model choice, parameter estimation and caveats. *Geophysics Journal International* 136, 357–372.
- Cowie, P.A., Knipe, R.J., Main, I.G., 1996. Introduction to the special issue. *Journal of Structural Geology* 18, pp. v–xi.
- Dee, S.J., Yielding, G., Freeman, B., Healy, D., Kuznir, N.J., Grant, N., Ellis, P., 2007. Elastic dislocation modelling for prediction of small-scale fault and fracture network characteristics. In: Lonergan, L., Jolly, R.J.H., Rawnsley, K., Sanderson, D.J. (Eds.), *Fractured Reservoirs*. Geological Society Special Publications, vol. 270, pp. 139–155.
- Davy, P., 1993. On the frequency-length distribution of the San Andreas fault system. *Journal of Geophysical Research* 98, 12141–12151.
- Gillespie, P.A., Walsh, J.J., Watterson, J., 1992. Limitations of dimension and displacement data from single faults and consequences for data analysis and interpretation. *Journal of Structural Geology* 14, 1157–1172.

- Gillespie, P.A., Walsh, J.J., Watterson, J., Bonson, C.G., Manzocchi, T., 2001. Scaling relationships of joint and vein arrays from The Burren, Co. Clare, Ireland. *Journal of Structural Geology* 23, 183–201.
- Hardacre, K.M., Cowie, P.A., 2003. Variability in fault size scaling due to rock strength heterogeneity: a finite element investigation. *Journal of Structural Geology* 25, 1735–1750.
- Heffer, K.J., Bevan, T.G., 1990. Scaling Relationships in Natural Fractures: Data, Theory and Applications. SPE paper 20981. Presented at the Society of Petroleum Engineers Europec 90 meeting, The Hague, Holland, Oct 1990.
- King, G.C.P., 1978. Geological faults: fracture, creep and strain. *Philosophical Transactions of the Royal Society of London A* 288, 197–212.
- Laslett, G.M., 1982. Censoring and edge effects in areal and line transect sampling of rock joint traces. *Mathematical Geology* 14, 125–140.
- Maerten, L., Gillespie, P., Daniel, J.-M., 2006. Three-dimensional geomechanical modeling for constraint of subseismic fault simulation. *AAPG Bulletin* 90, 1337–1358.
- Mäkel, G.H., 2007. The modelling of fractured reservoirs: constraints and potential for fracture network geometry and hydraulic analysis. In: Jolley, S.J., Barr, D., Walsh, J.J., Knipe, R.J. (Eds.), *Structurally Complex Reservoirs*. Geological Society, London, Special Publications, vol. 292, pp. 375–404.
- Manighetti, I., King, G., Gaudemer, Y., Scholz, C., Doubre, C., 2001. Slip accumulation and lateral propagation of active normal faults in Afar. *Journal of Geophysical Research* 106, 13667–13696.
- Manzocchi, T., Heath, A.E., Palanathakumar, B., Childs, C., Walsh, J.J., 2008. Faults in conventional flow simulation models: a consideration of representational assumptions and geological uncertainties. *Petroleum Geoscience* 14, 91–110.
- Manzocchi, T., Walsh, J.J., Nicol, A., 2006. Displacement accumulation from earthquakes on isolated normal faults. *Journal of Structural Geology* 28, 1685–1693.
- Marrett, R., Allmendinger, R.W., 1991. Estimation of strain due to brittle faulting: sampling of fault populations. *Journal of Structural Geology* 13, 735–738.
- Marrett, R., Ortega, O.J., Kelsey, C.M., 1999. Extent of power-law scaling for natural fractures in rock. *Geology* 27, 799–802.
- Mendenhall, W., Scheaffer, R.L., Wackerly, D. D., 1986. *Mathematical statistics with applications*, third ed. PWS Publishers, Boston, USA.
- Meyer, V., Nicol, A., Childs, C., Walsh, J.J., Watterson, J., 2002. Progressive localisation of strain during the evolution of a normal fault system. *Journal of Structural Geology* 24, 1215–1231.
- Moriya, S., Childs, C., Manzocchi, T., Walsh, J.J., 2005. Analysis of the relationships between strain, polarity and population slope for normal fault systems. *Journal of Structural Geology* 27, 1113–1127.
- Odling, N.E., 1997. Scaling and connectivity of joint systems in sandstone from Western Norway. *Journal of Structural Geology* 19, 1257–1271.
- Ortega, O.J., Marrett, R.A., Laubach, S.E., 2006. A scale-independent approach to fracture intensity and spacing measurement. *AAPG Bulletin* 90, 193–208.
- Pickering, G., Bull, J.M., Sanderson, D.J., 1995. Sampling power-law distributions. *Tectonophysics* 248, 1–20.
- Pickering, G., Bull, J.M., Sanderson, D.J., 1996. Scaling of fault displacement and implications for the estimation of sub-seismic strain. In: Buchanan, P.G., Nieuwland, D.A. (Eds.), *Modern Developments in Structural Interpretation, Validation and Modelling*. Geological Society, London, Special Publications, vol. 99, pp. 11–26.
- Scholz, C.H., Cowie, P.A., 1990. Determination of total strain from faulting using slip measurements. *Nature* 346, 837–839.
- Schultz, R.A., Soliva, R., Fossen, H., Okubo, C.H., Reeves, D.M., 2008. Dependence of displacement-length scaling relations for fractures and deformation bands on the volumetric changes across them. *Journal of Structural Geology* 30, 1405–1411.
- Soliva, R., Benedicto, A., 2005. Geometry, scaling relations and spacing of vertically restricted normal faults. *Journal of Structural Geology* 27, 317–325.
- Walsh, J.J., Bailey, W.R., Childs, C., Nicol, A., Bonson, C.G., 2003a. Formation of segmented normal faults: a 3-D perspective. *Journal of Structural Geology* 25, 1251–1262.
- Walsh, J.J., Childs, C., Imber, J., Manzocchi, T., Watterson, J., Nell, P.A.R., 2003b. Strain localisation and population changes during fault system growth within the Inner Moray Firth, Northern North Sea. *Journal of Structural Geology* 25, 197–208.
- Walsh, J.J., Watterson, J., 1988a. Dips of normal faults in British Coal Measures and other sedimentary sequences. *Journal of the Geological Society* 145, 859–873. London.
- Walsh, J.J., Watterson, J., 1988b. Analysis of the relationship between displacements and dimensions of faults. *Journal of Structural Geology* 10, 239–247.
- Walsh, J.J., Watterson, J., 1990. New methods for fault projection for coalmine planning. *Proceeding of the Yorkshire Geological Society* 49, 209–219.
- Walsh, J.J., Watterson, J., 1991. The importance of small-scale faulting in regional extension. *Nature* 351, 391–393.
- Walsh, J.J., Watterson, J., Yielding, G., 1994. Determination and interpretation of fault size populations: procedures and problems. In: Aasen, J.O. (Ed.), *North Sea Oil and Gas Reservoirs III*. Kluwer Academic Publishers, London, pp. 141–155.
- Watterson, J., Walsh, J.J., Gillespie, P.A., Easton, S., 1996. Scaling systematics of fault sizes on a large-scale range fault map. *Journal of Structural Geology* 18, 199–214.
- Westaway, R., 1994. Quantitative analysis of populations of small faults. *Journal of Structural Geology* 16, 1259–1273.
- Yielding, G., Needham, T., Jones, H., 1996. Sampling of fault populations using sub-surface data: a review. *Journal of Structural Geology* 18, 135–146.
- Zhang, L., Einstein, H.H., 2000. Estimating the intensity of rock discontinuities. *International Journal of Rock Mechanics and Mining Sciences* 37, 819–837.